remote sensing

MDPI

Article

Identifying Factors Influencing Surface Deformations from Underground Mining Using SAR Data, Machine Learning, and the SHAP Method

Konrad Cieślik [1,*], Wojciech Milczarek [2], Ewa Warchala [3], Paweł Kosydor [3] and Robert Rożek [3]

[1] trainAI sp. z o.o., Cegielniana 4a/15, 30-404 Kraków, Poland
[2] Department of Geodesy and Geoinformatics, Faculty of Geoengineering Mining and Geology, Wroclaw University of Science and Technology, Wybrzeże Wyspiańskiego 27, 50-370 Wrocław, Poland; wojciech.milczarek@pwr.edu.pl
[3] Department of Resource Management, KGHM Polska Miedź S.A., M. Skłodowskiej-Curie 48, 59-301 Lubin, Poland; ewa.warchala@kghm.com (E.W.); pawel.kosydor@kghm.com (P.K.); robert.rozek@kghm.com (R.R.)
* Correspondence: konrad.cieslik@trainai.io

Abstract: The article presents the results of significance analyses of selected mining and geological variables for an area of underground mining activity. The study area was a region of an underground copper ore mine located in southwest Poland. The input data consisted of satellite radar data from the Sentinel 1 mission as well as mining and geological data. The line-of-sight subsidence, calculated with the use of the small baseline subset method and arranged in time series, was decomposed to extract the vertical component. The significance analysis of individual variables for the observed surface subsidence was performed using the SHapley Additive exPlanations method for the XGBoost machine learning model. The results of the analysis showed that the observed ground surface subsidence velocities were most influenced by the thickness of the PZ3 layer, which is located approximately 200 m above the roof of the mined seam, the thickness of the seam, and the timing of mining. It was also found that the proposed model was able to detect a nonlinear relationship between the analyzed excavations. The most significant influence on ground subsidence over mine excavations are mining parameters such as the spatially averaged thickness of the deposit and the time since liquidation of the deposit. The proposed approach can be successfully employed in planning both mining operations and mine closure in such a manner that the environmental impact is minimized.

Keywords: SHAP method; Sentinel-1; SAR data; mining deformations; machine learning

check for updates

Citation: Cieślik, K.; Milczarek, W.; Warchala, E.; Kosydor, P.; Rożek, R. Identifying Factors Influencing Surface Deformations from Underground Mining Using SAR Data, Machine Learning, and the SHAP Method. *Remote Sens.* **2024**, *16*, 2428. https://doi.org/10.3390/rs16132428

Academic Editor: Kamran Esmaeili

Received: 8 May 2024
Revised: 21 June 2024
Accepted: 24 June 2024
Published: 2 July 2024

Copyright: © 2024 by the authors. Licensee MDPI, Basel, Switzerland. This article is an open access article distributed under the terms and conditions of the Creative Commons Attribution (CC BY) license (https://creativecommons.org/licenses/by/4.0/).

1. Introduction

Monitoring the effects of mining activity on the ground surface is a key issue in mining site protection. Ground surface subsidence may be particularly dangerous in urban areas, where it may pose a threat to both the ground-level and underground infrastructure [1,2]. Underground mining exploitation causes voids to be created in the rock mass. Some of these voids are then filled by the rock masses that move due to gravity, leading to the development of deformations on the ground surface. A number of surveying methods are used to determine the extent and magnitude of subsidence caused by mining. Among the most important are classical surveying methods such as precise leveling [3,4] and global navigation satellite systems (GNSS) [5–7]. At the same time, in the last decade, remote sensing and photogrammetric methods have been increasingly used. The literature contains numerous studies on the use of unmanned aerial vehicles (UAVs) [8–10], laser scanning: ground [11,12] and airborne [13,14], and methods for processing satellite radar data. According to the authors, SAR time series methods, such as the persistent scatterer interferometric (PSI) method [15–18], small baseline subset (SBAS) method [4,19,20], offset-tracking method (OTM) [21,22], and, to a more limited extent, ground-based radar

interferometry [23,24], are particularly noteworthy. Remote sensing ground observation techniques are characterized by high data acquisition rates, which are often several days or even less. Spatial resolution is another important consideration in selecting optimal surface monitoring solutions. In the case of SAR data, it is also not insignificant that this type of data provides the opportunity to observe the Earth's surface regardless of the time of day and weather conditions.

InSAR methods provide large sets of high-resolution data that can be used in the increasingly common machine learning (ML) [25–29] based analyses. A sample dataset from the Sentinel 1A/B missions can be used as an example. The Sentinel 1A satellite was launched in 2014. In 2016, a second, twin satellite with SAR instrumentation was placed in low orbit: Sentinel 1B, which provided data until the end of 2021. This constellation of satellites provided data with an interval of 6 days, or 12 days for a single satellite. For any mining area in Europe, it is possible to generate a time series of more than 450 time periods. Analysis of the time series (e.g., based on the SBAS method) makes it possible to observe changes on the surface with sampling of the order of 30 × 30 m, and the imaging itself has dimensions of about 200 × 280 km. Analysis of terrain and seasonality of such large datasets is practically possible with the use of selected ML algorithms. What is more, linking the results of SAR time series with ML also makes it possible to develop models that can forecast surface [26,28,30,31] movements.

When forecasting phenomena with the use of machine learning, the key element is to determine the significance of input data so as to find which data are of the greatest influence at the forecasting stage. Such an analysis provides important information about the relationships and patterns in the data, and thus helps to interpret the model, select its features, and understand the factors that have a decisive impact on the accuracy of the forecast.

The use of machine learning algorithms together with high-resolution SAR data allowed the identification of the parameters that the authors believe to have a major effect on the extent and range of ground surface subsidence observed using InSAR techniques. In the research known in the literature, the extent to which a particular layer of rock mass affects the ground surface was analyzed with the use of numerical methods [32,33]. The finite element method [34,35], the discrete element method [36], or the finite difference method [37] require detailed knowledge of the geological structure of the rock mass as well as correctly defined physical and mechanical properties of the rock layers. Such models also require the adoption of precise initial conditions and adequate consideration to the complexity of the processes occurring in the rock mass due to mining exploitation, as well as its impact on the surroundings. The use of machine learning algorithms together with SAR data in order to identify factors that influence mining deformations on the ground surface is a new idea that in the future may, to some extent, become an alternative to the currently used numerical methods.

Similarly, identifying the significance of geological layers and the impact of mining activity in the context of using machine learning in predictions of mining-induced ground-surface deformations is a relatively new problem, insufficiently addressed in the literature. The existing publications are concerned with related issues, such as tunneling [38–40] or the impact of drainage on the land surface [41,42]. One article [43] discusses the application of selected machine learning algorithms and automatic machine learning (AutoML) technologies in predicting maximum ground subsidence in the construction of tunnels using earth pressure balance tunnel boring machines (EPB TBM). The research also included feature selection using the Shapley Additive exPlanations (SHAP) correlations and algorithm to identify the most significant input parameters. The analyzed features included soil type, torque, rock mass thickness, groundwater level, and tunnel deviation off course, which were found to have a significant impact on the surface subsidence process. In the work of Kannangar [44], selected machine learning algorithms, including SHAP, were used to investigate the impact of different feature selection methods on predictions of tunneling-induced subsidence. Nafees et al. [45] used ML in combination with SAR data and a range

of geological and terrain parameters for landslide susceptibility mapping. They tested which parameters are most related to landslides using correlation analysis and feature importance from the random forest model. They obtained very similar results with both of these methods, showing that slope followed by aspect and rainfall with a minute margin have the greatest impact. Another article [46] presents the results of research aimed at preparing a comprehensive map of ground surface subsidence due to groundwater by integrating SAR data and machine learning algorithms.

In the article, we focused on employing machine learning models to find key mining and geological factors influencing ground surface subsidence directly above mining excavations. Surface subsidence velocities identified with the use of the SBAS method [47] served as the function of the prediction target for the models. The study area was defined within the limits of an underground copper ore mining region. The aim of our article is to evaluate the feasibility of using the SHAP algorithm together with SAR data in determining the relevance of geological-mining factors on the size and extent of mining deformations. Due to the use of feature importance from machine models [48], it was possible to quickly identify key variables and perform a deeper analysis. The analysis methodology proposed in this article can significantly accelerate and automate the detection of the most important mining and geological factors that influence the extent and velocity of ground subsidence above underground mining excavations. Such an approach may be useful in planning the progress of mining fronts when the objective is to minimize the negative impact of mining on the ground surface.

2. Study Area

The Legnica–Glogow Copper Belt (LGCB) is located in the area of the Fore Sudetic monocline, in southwest Poland (Figure 1), whose structure was shaped during the Cimmerian and Laramie movements. The bedrock of the monocline consists of metamorphic formations of the Proterozoic (mainly gneisses and amphibolites) lying at a depth of more than 1400 m. The copper ore deposit in this region is located in the roof part of the Rotliegend and in the floor part of the Zechstein. The deposit is one of the largest polymetallic deposits in the world. Currently, copper ore mining is carried out at a depth of more than 1100 m below the ground surface. The area is rich in copper ore, which is currently mined from six deposits by three mining plants: Lubin, Rudna, and Polkowice–Sieroszowice, at depths which occasionally exceed 1200 m. All mines are part of KGHM Polska Miedź SA, one of the largest copper producers in the world. The area is one of the most important mining regions in Poland. The first mentions of copper mining in the area of Legnica and Głogów date back to the 13th century. The mining operations are performed with the retreat room and pillar method with hydraulic backfill (in the case of areas requiring surface protection). Copper ore in the LGCB region is generally formed in three types of rocks: Rotliegend and Grauliegend sandstones, Zechstein copper shales, and carbonate rocks. Rocks of the last type, which are typically found in the roofs of the excavations, show high strength and ability to accumulate elastic energy, and therefore they facilitate mining tremors.

The study area was defined in the region where copper ore has been mined with varying intensity for more than ten years. The central part of the analyzed area comprises a subsidence basin, formed as a direct result of mining activity.

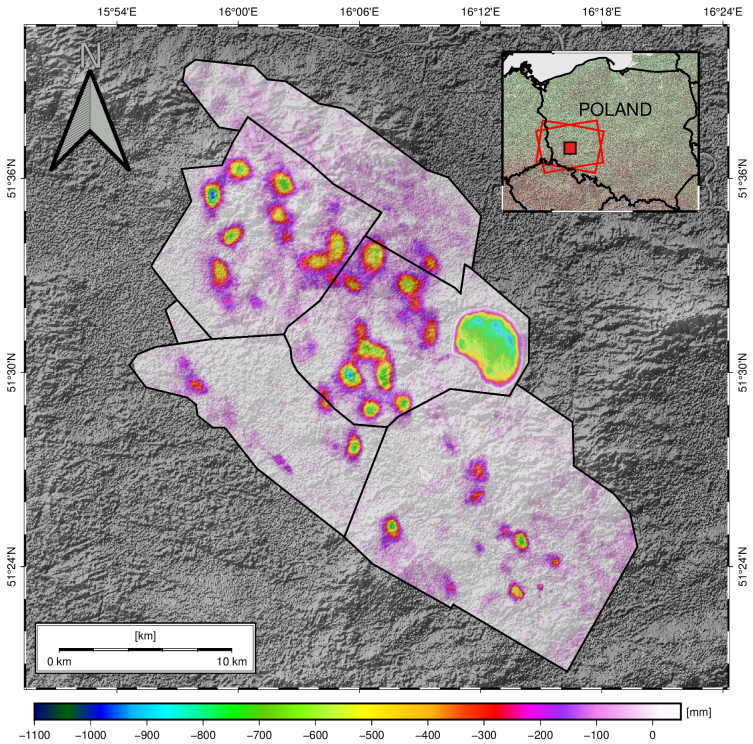


Figure 1. Location of the LGCB mining areas with plotted subsidence of the ground surface for the period November 2014–December 2022 calculated from SAR data using the SBAS method from two paths: 22 and 73 (red polygons on the small map).

3. Data and Methodology

3.1. Data

In the calculations, we used SAR data from the Sentinel 1 mission operating at C-band. Access to the data is provided free of charge, and the frequency of acquisition of successive SAR images and the resolution of the data are completely sufficient to analyze long-term subsidence of the ground surface caused by underground mining operations. The long-term subsidence was identified on the basis of data from both the descending path and the ascending path. The calculations of the interferograms were based on two-pass processing with the use of GMTSAR ver. 6.2.2 [49]. Phase unwrapping was performed with the Snaphu ver. 1.4.2 application [50]. Wave phase correction in relation to the ground surface was performed with the data from Shuttle Radar Topography Mission (SRTM) version 1 [51]. The enhanced spectral diversity (ESD) algorithm was not used at the preprocessing stage. The line-of-sight (LOS) displacement calculations were performed by simultaneously employing the SBAS method and the GACOS method [52] for reducing the influence of the troposphere. The decision to implement tropospheric corrections in the SBAS time series analyzed was motivated by previous studies in the area. A previous paper [53] showed that the use of tropospheric corrections significantly reduces the global (with respect to the range of SAR data) shift in the interferometric phase. The time span for the presented research was over 8 years, from November 2014 until December 2022. The total number of calculated interferograms was similar for the two paths and amounted to over 2200 (Table 1 and Figure 2). Decomposition of the LOS signal was performed according to the methodology presented in Milczarek et al. [54]. In the analyses using the SHAP method, we used only the vertical component of the displacements.

Table 1. Background information on SAR data and SBAS time series results used in forecasting.

Calculation Period	**November 2014–December 2022**	
sensor	Sentinel 1A/B	
orbit number/IW	22/IW2	73/IW2
orbit type	descending	ascending
number of SAR images	399	393
mean period between images	12 days (November 2014 to July 2016 and January 2022 to now); 6 days (August 2016–December 2021)	
spatial and time base	50 m/50 days	
number of interferograms	2286	2255

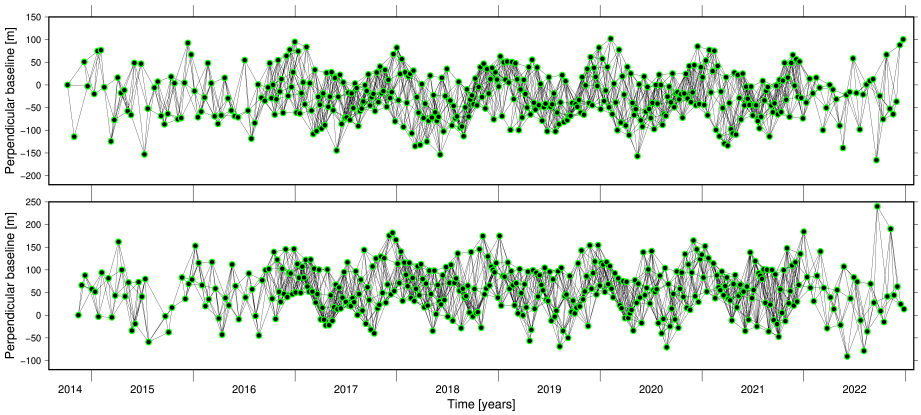


Figure 2. Baseline plot for the two SAR datasets obtained from path 22 (**above**) and path 73 (**below**). The analyzed period spanned the years from 2014 to the end of 2022.

InSAR calculations were performed for the entire operating area of the company. Variable analyses, however, were performed for a selected area of 2.5 × 2.4 km (Figure 3). Example results of surface subsidence along the specified profile are shown in Figure 4. Basic lithological data of the analzed area are shown in Figure 5. In addition to SAR data, the analyses used geological data about the thickness of geological layers overlying the mining excavations (Figure 6) and about the locations of local tectonic faults. The mining data included spatial information about the limits of the mining area and the duration of the mining activity (Table 2).

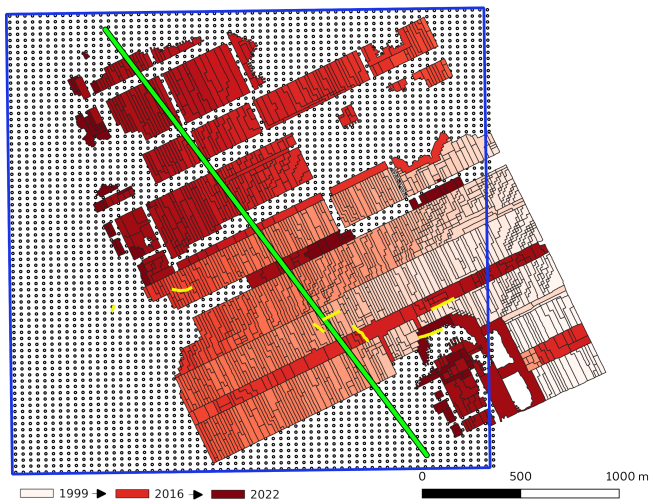


Figure 3. Location of the study area: red marks the boundaries of the area, the gray dots represent the the results array of SBAS time series calculations, and the exploited deposit is marked with gray polygons. The green line shows the path of the geological profile, and and the yellow lines represent local tectonic dislocations.

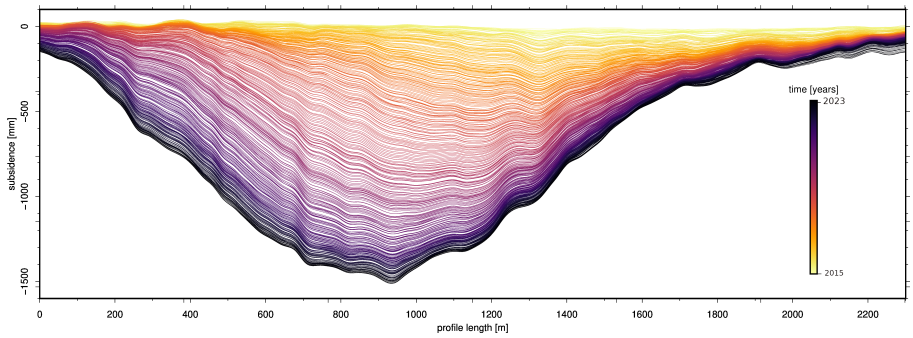


Figure 4. Results of SAR data calculations using the SBAS method–cumulative subsidence of the ground surface along the profile marked in Figure 3; the results cover the period from November 2014 to December 2022.

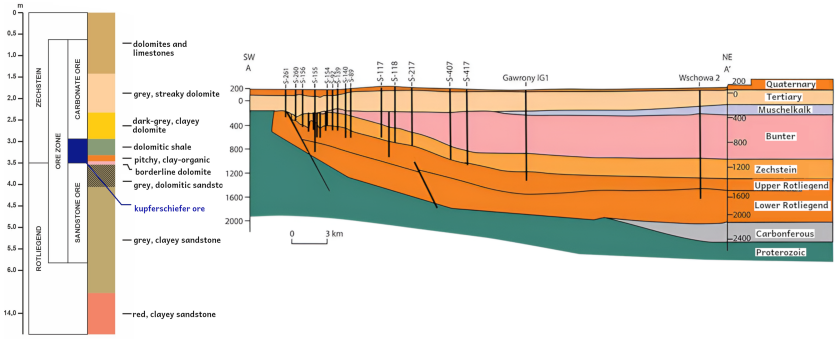


Figure 5. (**Left**): Lithological profile of the Fore–Sudetic Monocline copper ore deposit and (**right**): geological cross-section through copper ore deposits in the Fore–Sudetic Monocline (adapted from [55]).

All geological, tectonic, and mining data used in the analyses were obtained from the mining company KGHM Polska Miedź. These are real sourced data from the analyzed area.

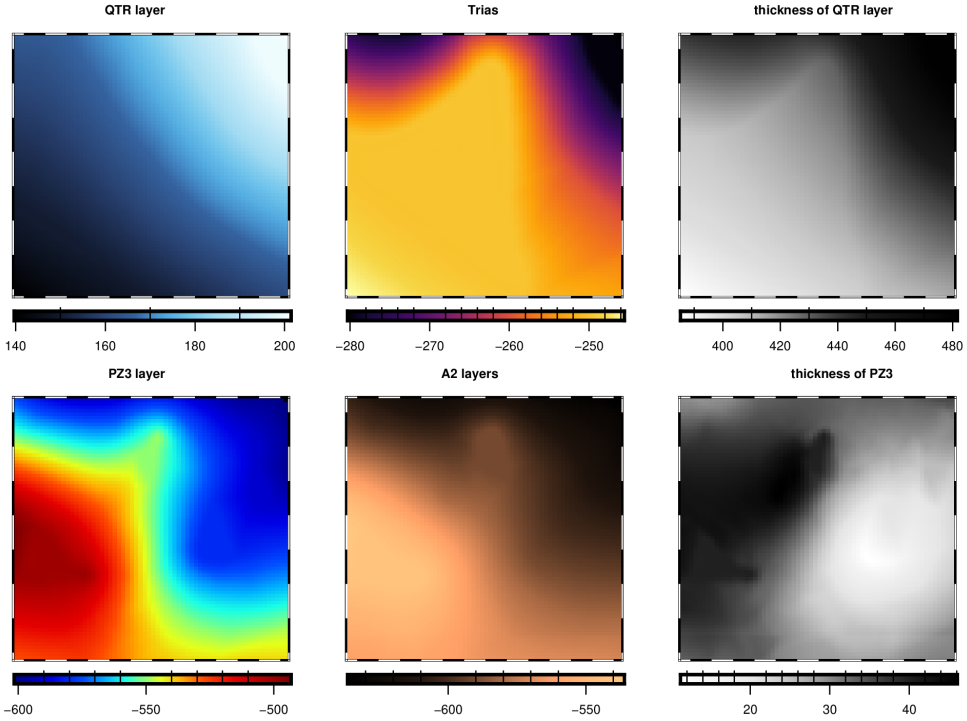


Figure 6. Depth of geological strata (**left** and **centre**) and thickness between them (**right**).

Table 2. Summary of geological and mining data used to train the XGBoost model and list of variables used in SHAP calculation.

Feature Name	Description
Depth_layer_X	Depth of the layer "X" below the observation point (where X is a specific layer) [m]
Thickness_layer_X	Thickness of the layer "X" below the observation point (where X is a specific layer) [m]
distance_to_fault_Y	Horizontal distance from the observation point to a specific fault location "Y" [m]
closest_fault_distance	Horizontal distance from the observation point to the to the closest fault [m]
mined_thickness	Thickness of the deposit layer which was mined [m]
depth_deposit_layer	Deposit layer depth and thickness below the observation point [m]
thickness-deposit_layer	Thickness of the deposit layer
salt_body [1]	Existence of the salt body below the observation point [bool]
t0	Time in days since deposit was extracted below the observation point (negative values means number of days before extraction) [days]
t0_IDW_Z	Averaged t0 calculated for a specific observation point with inverse distance weighting based on 'Z' nearest points
mined_thickness_IDW_Z	Averaged mined thickness calculated for a specific observation point with inverse distance weighting based on 'Z' nearest points

List of variables used in SHAP calculation

1. *t0*	9. *depth_deposit_layer*	17. *distance_to_fault_6*	25. *thickness-Trias*
2. *depth_PZ3*	10. *depth_NA1*	18. *distance_to_fault_7*	26. *thickness-CA2*
3. *salt_body*	11. *distance_to_fault_3*	19. *depth_A2*	27. *thickness-A2*
4. *depth_PZ4*	12. *distance_to_fault_2*	20. *closest_fault_distance*	28. *thickness-PZ3*
5. *depth_BS*	13. *depth_CA2*	21. *thickness-NA1*	29. *t0_IDW_50*
6. *mined_thickness*	14. *distance_to_fault_1*	22. *thickness-PZ4*	30. *t0_IDW_10*
7. *depth_Trias*	15. *distance_to_fault_5*	23. *thickness-deposit_layer*	31. *mined_thickness_IDW_50*
8. *depth_QTR*	16. *distance_to_fault_4*	24. *thickness-QTR*	32. *mined_thickness_IDW_10*

[1] —information on salt concerns only the spatial extent of occurrence.

3.2. Methodology

The main goal of this research was to determine whether SAR data and machine learning can be used to prepare reliable, long-term forecasts and simulations of the impact of mining on the ground surface. The prediction target was set to the subsidence velocities rather than the accumulated subsidence values over time. A flow chart of the proposed methodology for analyzing the significance of geological-mining parameters using the SHAP method supported by SBAS series is shown in Figure 7.

As a result, the prediction signal after conversion is stationary (without a long-term trend) and a wider range of ML models could be employed, including those based on decision trees (Figure 8). Cieślik and Milczarek [28] demonstrated that this effect is not possible when the prediction target is set to the cumulative subsidence values.

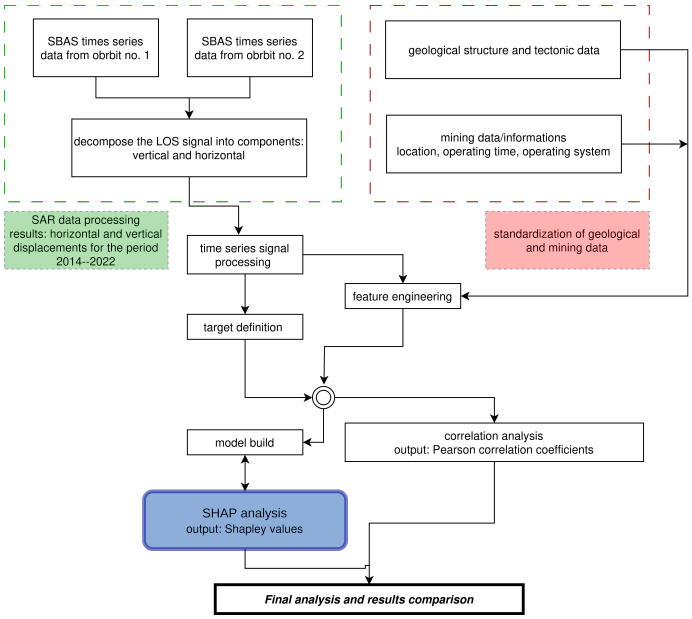


Figure 7. The flow chart of the proposed methodology for analyzing the significance of geological-mining parameters using the SHAP method supported by SBAS series.

The first step was to process the SAR data from the two independent paths into cumulative LOS displacements. The next step was the decomposition of the LOS signal, and the result was horizontal and vertical displacements in the E–W direction. The vertical component was subjected to signal processing procedures. This procedure had two main objectives. The first goal was to raise the signal-to-noise (S/N) ratio by removing high-frequency noise (Figure 8). As a result, the de-noised prediction signal became more stable. The second goal was to convert from the subsidence domain to the subsidence velocity domain. This made it possible to include the temporal aspect of the formation of mine workings in the analyses since the velocity corresponds to changes in the deformation of the ground at a given moment (Figure 9).

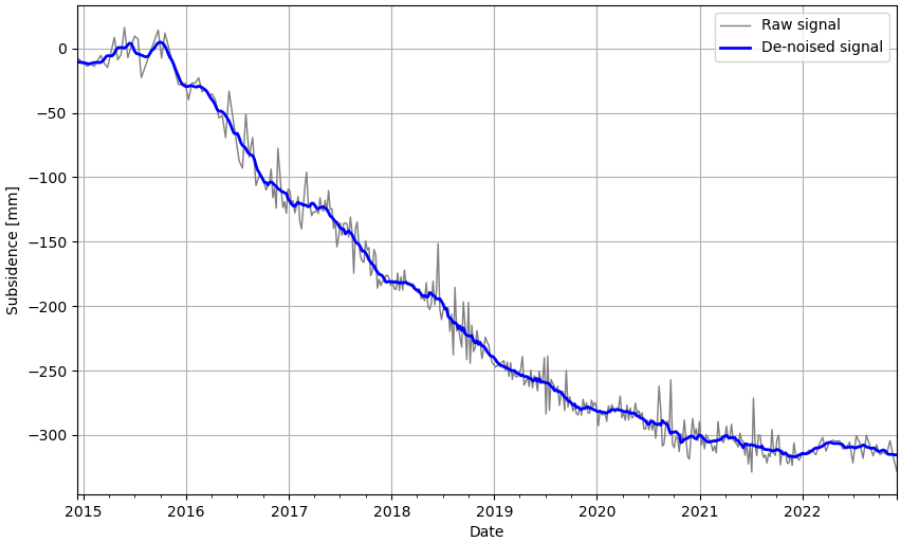


Figure 8. Conversion of subsidence determined from InSAR time series to the velocity domain with simultaneous removal of high-frequency noise.



Figure 9. Schematic diagram of converting the SBAS time series signal from the subsidence domain (**top**) to the velocity domain (**bottom**).

The results obtained in this way were used as a target for ML models. In parallel with the SAR data calculations, feature engineering of geological-mining data was performed, which is a standard approach when preparing data for models to be used in ML. This procedure included, among other things: (1) normalization of the data, (2) calculation of the thickness of the geological layers (Figure 6), (3) calculation of distances to faults, (4) spatial averaging of the geological and mining data, and (5) calculation of parameters related to mining time. The data prepared in this way were used to: (I) to check their correlation with subsidence velocity and (II) to build a ML model whose purpose was to forecast subsidence velocity.

The crucial step was to perform analyses using the SHAP algorithm to extract information on which geological-mining data had the greatest impact on the model's predictions. The final step was to analyze the mining-geological parameters that were indicated by SHAP as the most significant with the results of the correlation analysis.

From the perspective of scientific research, the prediction problem was treated as a supervised learning regression, where the main prediction target was the rate of surface subsidence due to underground mining exploitation, in both space and time. The training dataset contained randomly selected spatial points for 75% of the data acquisition timespan. The remaining part of the data was used to validate the results. XGBoost [56] was selected as the best machine learning algorithm and was used to analyze the parameters indicated by the model to be the most significant.

The significance of the impact of individual variables on ground surface subsidence was assessed with the SHAP method. SHAP is based on the Shapley value concept from the cooperative game theory [57] and provides a unified and mathematically sound approach to interpreting both the results of complex models and the contribution of each input function to the final forecast [58]. The SHAP value is calculated from the following equation [59]:

$$\phi_i = \sum_{S \subseteq F \setminus \{i\}} \frac{|S|!(F - |S| - 1)!}{F!} [f_x(S \cup i) - f_x(S)]$$

where ϕ_i represents the SHAP value for the feature i, F is the set of all features, S is a subset of F that does not include feature i, $|S|$ represents the number of features in a subset of S, The notation $F \setminus \{i\}$ means the set F without i and the value function is represented by $f(\cdot)$. With the use of the above equation, the contribution of each feature can be calculated, and, by comparing the model results with and without the feature, all possible combinations of features can be taken into account. Importantly, the complexity of computing SHAP values increases exponentially with the number of features, and thus the processing of large feature sets requires significant computing power. Efficient calculations of SHAP values for practical purposes are possible with the use of approximation algorithms and specialized libraries.

Based on the SHAP method, selected features (geological and mining data) were plotted into importance charts, which show the relative importance of each feature in the prediction. SHAP may also allow individual forecasts to be explained by assigning a contribution score to each feature, indicating its impact on the final forecast.

4. Results

The calculation results describing the influence of the most important parameters on the performance of the model are presented in Figure 10, in the form of SHAP values. It should be noted here that the proposed models (1–3) are able to detect nonlinear and discontinuous relationships. On the other hand, a correlation does not always mean causality. Low importance of some parameters does not mean that they are insignificant. For example, they may have insufficient variance and therefore they may not provide additional information to the model.

Figure 10 shows the average absolute SHAP values (on the left) as a bar chart and a bee swarm chart (on the right), in which each point is a single observation in space and time, and the color indicates the value of a given parameter.

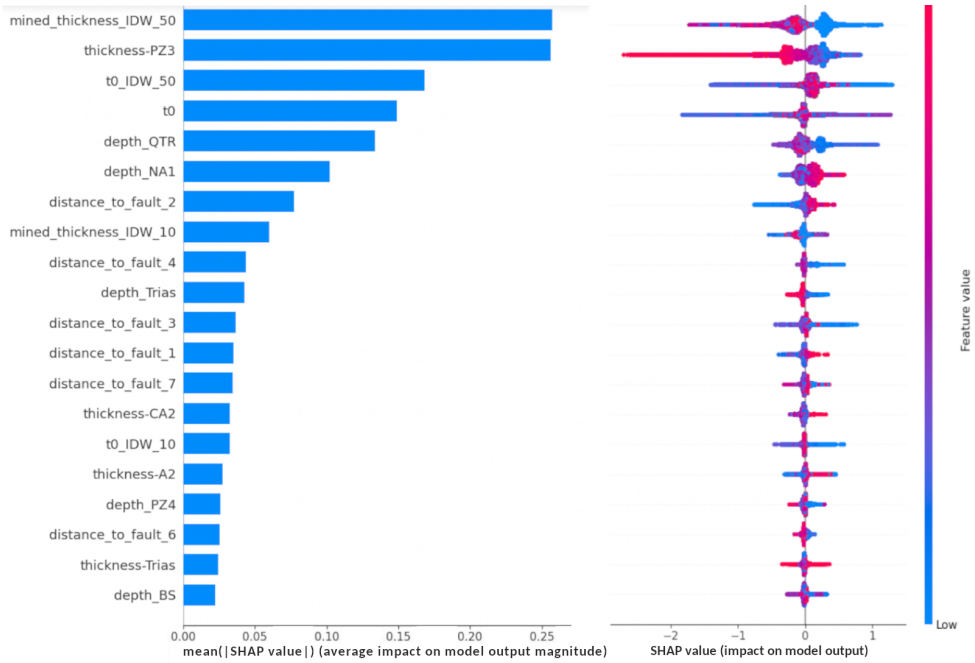


Figure 10. Effect/significance of individual parameters on the performance of the model (**Left**: bar chart of mean SHAP value. **Right**: set of bee swarm graphs, where each dot corresponds to an individual point in space and time in the study. The position of a dot on the x-axis shows the effect of that feature on the model's prediction for that point in time. When multiple dots land at the same x position, they are pooled to show density). The figure shows the results for 20 of the 32 variables (see Table 2). The values of the remaining 12 variables were below 0.25 and were considered insignificant.

The highest average SHAP values for the model were assigned to the *mined_thickness_IDW_50* and *thickness_layer_PZ3* parameters (∼0.25). The bee swarm chart shows that, in both cases, high values of the two parameters negatively influence the predictions of the model, i.e., they mean higher subsidence rates. Interestingly, *layer_PZ3* is not located directly above the mining site, but rather an average of 186 m above it. This result is consistent with the assumptions based on the rock mass mechanics in the area, as these layers are subject to deflection and the overlying layers follow this deflection.

The next two significant parameters are the time to liquidate the exploited parcel (*t0*) and its spatially averaged version (*t0_IDW_50*). In this case, the values closer to zero also have a negative impact on the predictions (higher subsidence rates). However, here, the time bee swarm charts are not clear.

In Figure 11, the identified four most significant variables are plotted as graphs of the relationship between a given variable (x-axis) and its SHAP value (y-axis), which represents its impact on the predictions of the model. Additionally, the parameter forming the strongest interaction is marked in color.

As can be seen, the *mined_thickness_IDW_50* parameter has the greatest impact (high absolute SHAP values) on the model when the *thickness_layer_PZ3* values are simultaneously high (red). The highest absolute SHAP values of the *thickness_layer_PZ3* parameter are observed when it has high values and simultaneously the time *t0* is close to zero. The variables related to liquidate the exploited parcel time have the greatest impact on the model when they are close to zero and when the *thickness_layer_PZ3* value (for the *t0_IDW_50* parameter) and the *mined_thickness_IDW_50* value (for *t0*) are also high.

In order to understand the impact of the above parameters on the prediction, they were additionally analyzed as a function of the target, i.e., the subsidence rate.

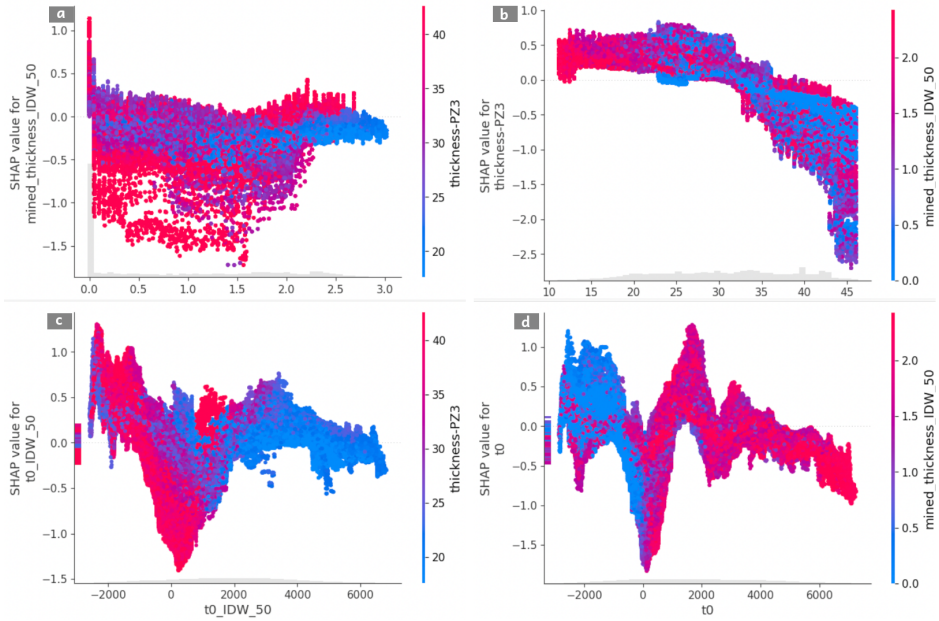


Figure 11. Relationship diagram of the four (**a**—*mined_thickness_IDW_50*, **b**—*thickness_layer_PZ3*, **c**—*t0_IDW_50*, **d**—*t0*) most significant parameters (x-axis) and their SHAP values (y-axis), i.e., their influence on the model predictions. An additional color is used to indicate the parameter with which they form the strongest interaction.

The *thickness_layer_PZ3* and *t0* as a function of the target (subsidence rate) were visualized in the following form (Figure 12): the x-axis is the time to liquidate the exploited parcel, the y-axis is the thickness of *layer_4*, and the subsidence rate is indicated with different colors. The subsidence rate proves to be the highest in the period of time most closely preceding to liquidate the exploited parcel (x-axis). The above relationship shows that the subsidence rate increases together with the increasing thickness of *layer_PZ3*.

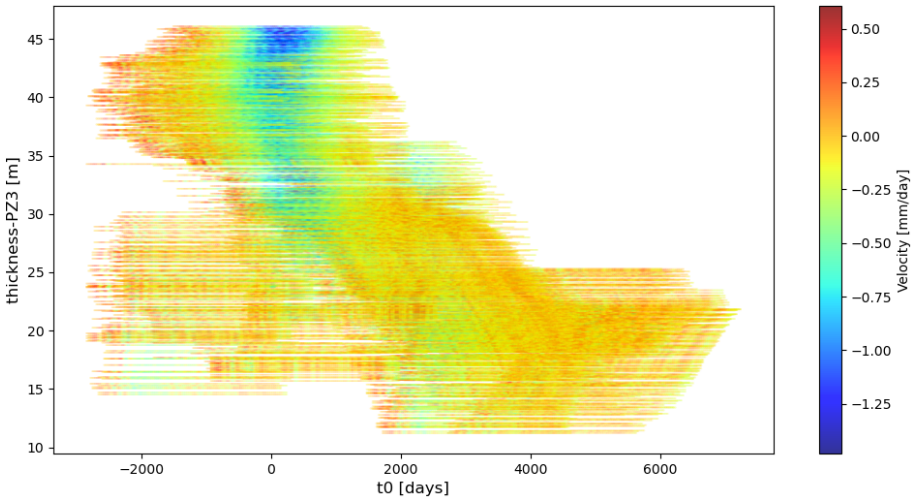


Figure 12. The relationship of subsidence velocity (color) with time to deposit liquidation and thickness of geological *layer_PZ3*.

As the prediction target varies with time, whereas geological parameters such as the layer thickness and depth are constant during the investigated period, a simple correlation analysis is not possible. In order to perform a correlation analysis, each measurement point was attributed a time point at which the subsidence rate was the highest.

Figure 13 below shows the correlation matrix for all the parameters. The highest subsidence rate is provided in the bottom row—the correlation coefficient values are sorted from lowest to highest.

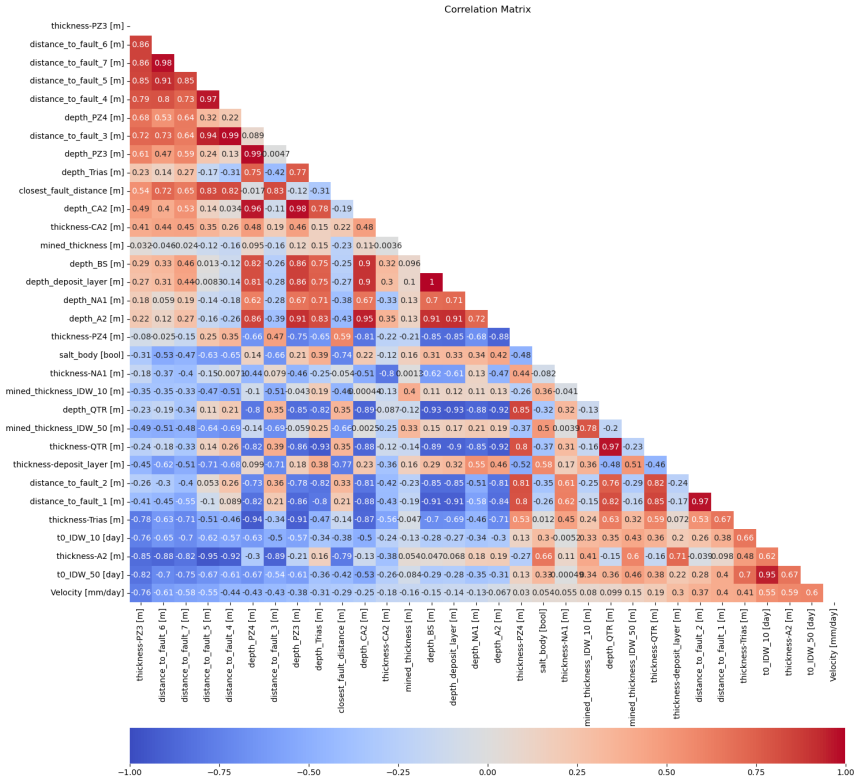


Figure 13. Matrix of correlation coefficients. Coefficients for the highest subsidence velocity are in the bottom row.

The correlation coefficient for the pair "highest rate −*thickness_layer_PZ3*" is −0.76, and this is the highest absolute value among all the subsidence rate pairs. This result is consistent with the machine learning model in which the thickness of *layer_PZ3* has the greatest impact on the predictions. However, the correlation coefficient of the mined thickness parameter (*mined_thickness_IDW_50*—spatially averaged) is very low (+0.15), also lower than many other parameters. This fact may indicate that the model was able to detect a nonlinear dependence of this parameter on the target function or that the parameter is not significant for the point in time with the highest subsidence rates. Therefore, further investigations focused in more detail on the following two parameters: *thickness_layer_PZ3* and *mined_thickness_IDW_50*.

Figure 14 is a spatial visualization in the form of a map and a cross plot of the *thickness_layer_PZ3* parameter with the highest subsidence rates. A strong linear relationship can be observed—greater layer PZ3 thickness correlates with higher subsidence rates.

As the InSAR data do not cover all of the mining activity periods for the study area, the spatial and correlation analyses were repeated after eliminating those measurement points in which mining operations were active before the acquisition of the first SAR data (November 2014).

Figure 15 shows that, although the points located in the south-eastern part of the study area have been removed, a strong correlation of the subsidence rate to the thickness of *layer_PZ3* can be still observed.

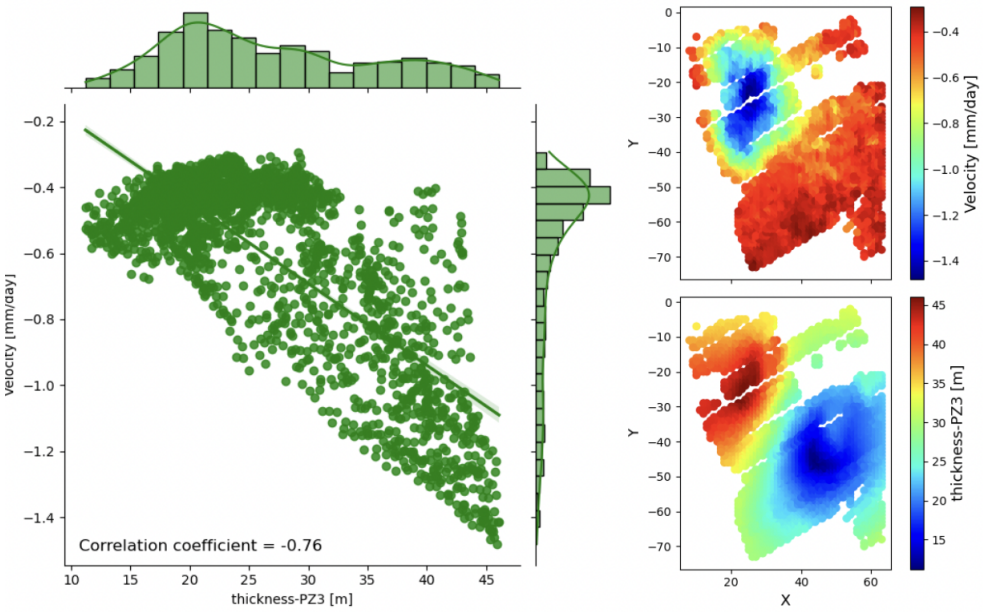


Figure 14. Comparison of the spatial distribution of the highest subsidence velocities (**top**) to the thickness of *geological layer_PZ3* (**left**). (**bottom**): correlation of the highest subsidence velocities to the thickness of *geological layer_PZ3*. Correlation coefficient = −0.76.

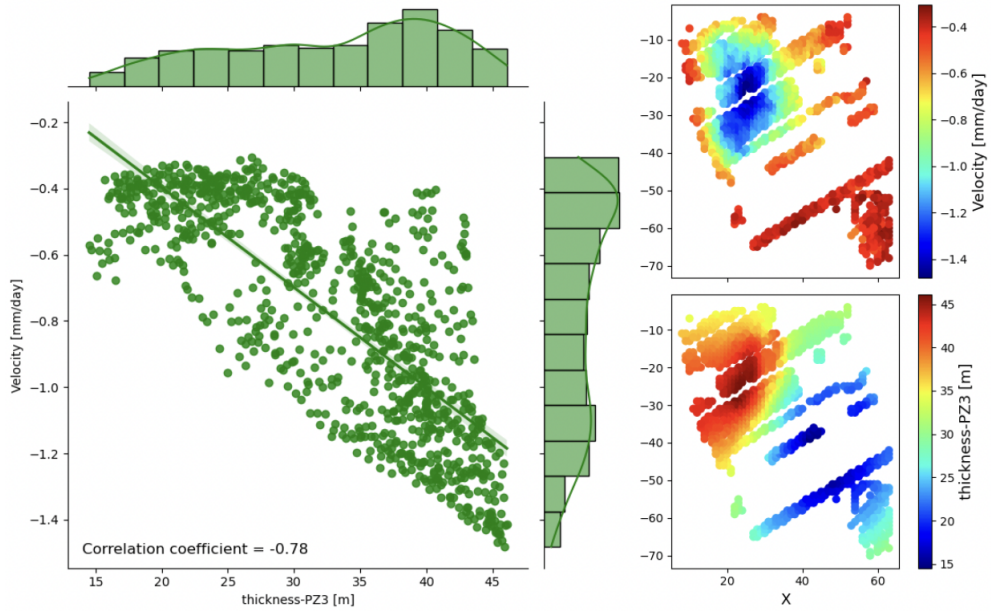


Figure 15. Comparison of the spatial distribution of the highest subsidence velocities (**top**) to the thickness of geological *layer_PZ3* (**left**) after elimination of measurement points for which exploitation took place before the collection of the first InSAR data (end of 2014). (**bottom**): relationship between the highest subsidence velocities (y-axis) and the thickness of geological *layer_PZ3* (x-axis) after elimination of measurement points for which exploitation took place before the collection of the first InSAR data (end of 2014). Correlation coefficient = −0.78.

Another of the investigated parameters that had a significant impact on the machine learning model was the thickness of the excavation in its spatially averaged form. Figure 16 shows this parameter in the form of a map and, for comparison, its non-averaged (raw) version.

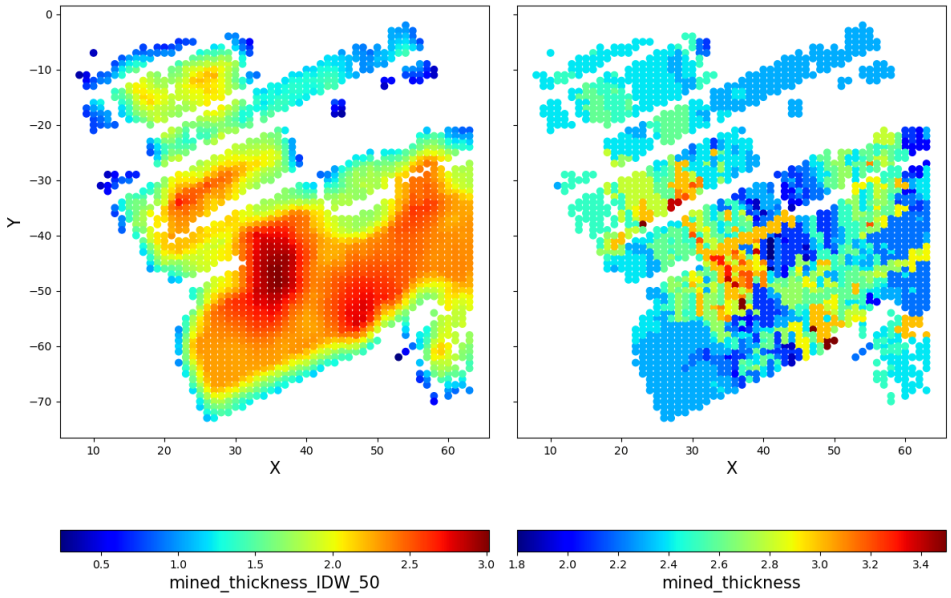


Figure 16. The thickness of the excavation [m] (**right**) and its averaged version after using IDW from 50 adjacent points (**left**).

In the case of the mined thickness, the correlation presented in Figure 17 is not as obvious as the correlation for the *layer_PZ3* thickness shown in Figure 8.

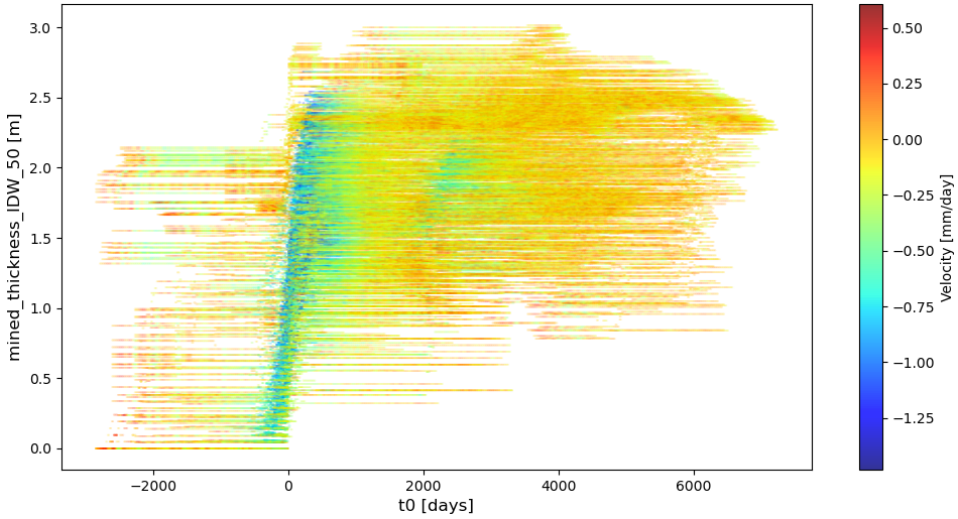


Figure 17. Relationship of subsidence velocity (color) to time to end of mining in the successive exploitation parcels of the deposit (x-axis) and spatially averaged (IDW 50 points) mine thickness (y-axis).

The data, spatially visualized in the form of a map, show that the largest mined thicknesses can be found in the southern part of the study area. The cross-plot visualization indicates the presence of two groups of points that behave differently (Figure 18). The first group consists of points with a minimum subsidence rate ranging from −2 to −3 mm/6 d, regardless of the mined thickness. The second group consists of points where a correlation exists between the subsidence rate and the mined thickness.

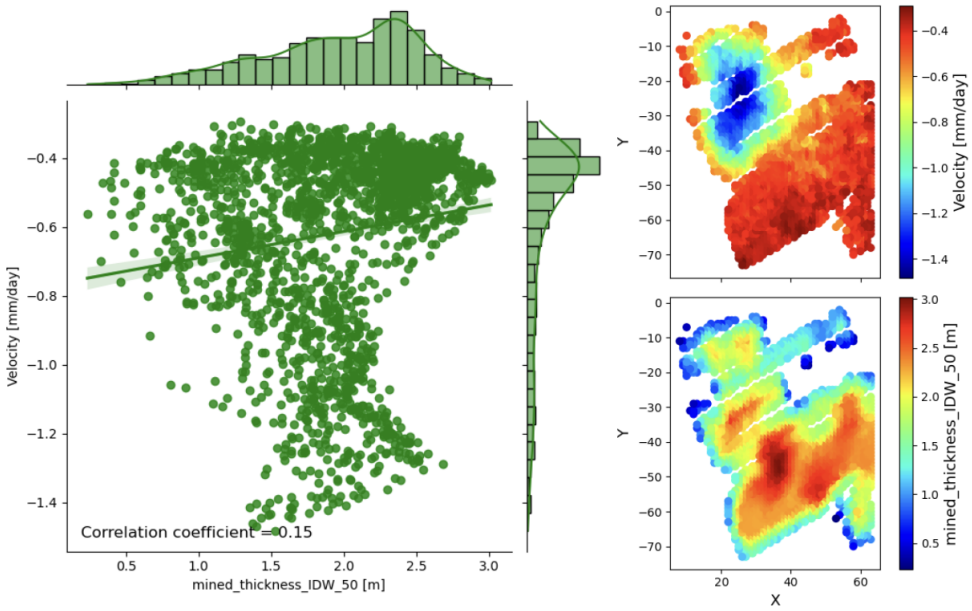


Figure 18. Comparison of the spatial distribution of the highest subsidence velocities (**top**) to the spatially averaged (IDW 50 points) thickness of the excavation (**left**). (**bottom**): relationship between the highest subsidence velocities (y-axis) and the spatially averaged (IDW 50 points) thickness of the excavation (x-axis).

As before, we eliminated all measurement points in which mining operations were active before the acquisition of the first InSAR data. Figure 19 shows the updated maps and the cross-plot after eliminating these points.

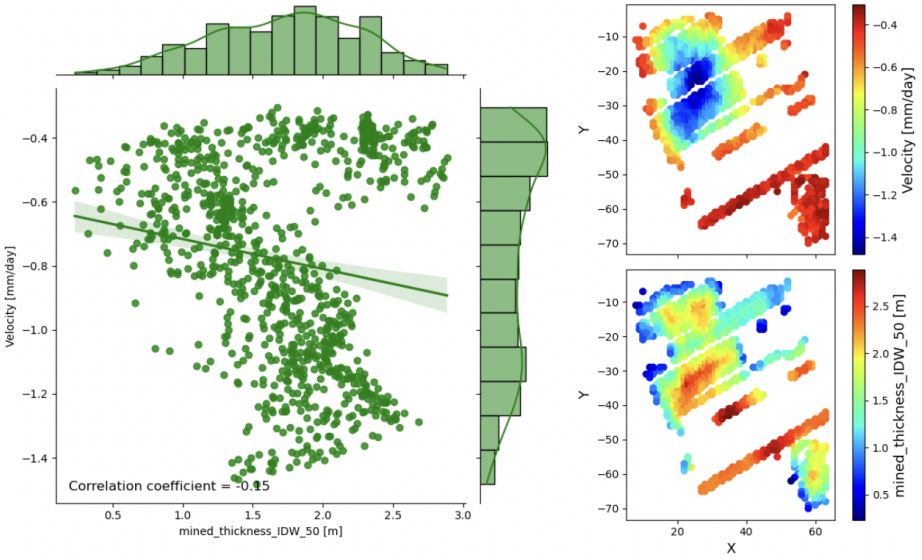


Figure 19. Comparison of the spatial distribution of the highest subsidence velocities (**top**) to the spatially averaged (IDW 50 points) thickness of the excavation (**left**) after elimination of measurement points for which mining took place before the collection of the first InSAR data (end of 2014). (**bottom**): relationship between the highest subsidence velocity (y-axis) and the spatially averaged (IDW 50 points) thickness of the excavation (x-axis) after elimination of measurement points for which exploitation took place before the collection of the first InSAR data (end of 2014).

After eliminating these points, a smaller group of points can be still identified, which show low subsidence rates regardless of the mined thickness (Figure 20). After being

marked, the points from the southern area indicate that the lower subsidence rates are located in the southern part of the study area, represented in orange in Figure 21, where *layer_PZ3* has smaller thicknesses.

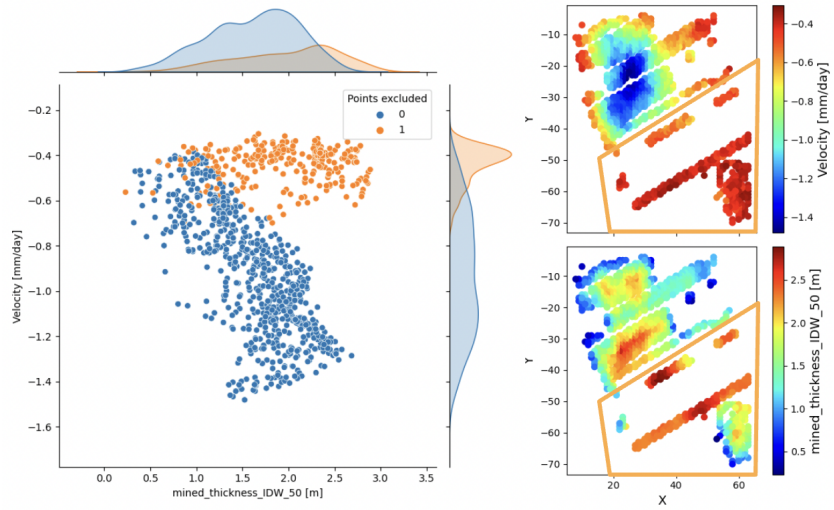


Figure 20. The relationship of the highest subsidence velocities (y-axis) (**top**) to the spatially averaged (IDW 50 points) thickness of the excavation (x-axis) (**left**) after elimination of measurement points for which mining occurred before the collection of the first InSAR data (end of 2014) (**bottom**). Points from the southern area are marked in orange on the cross plot and marked on the map with an orange rectangle.

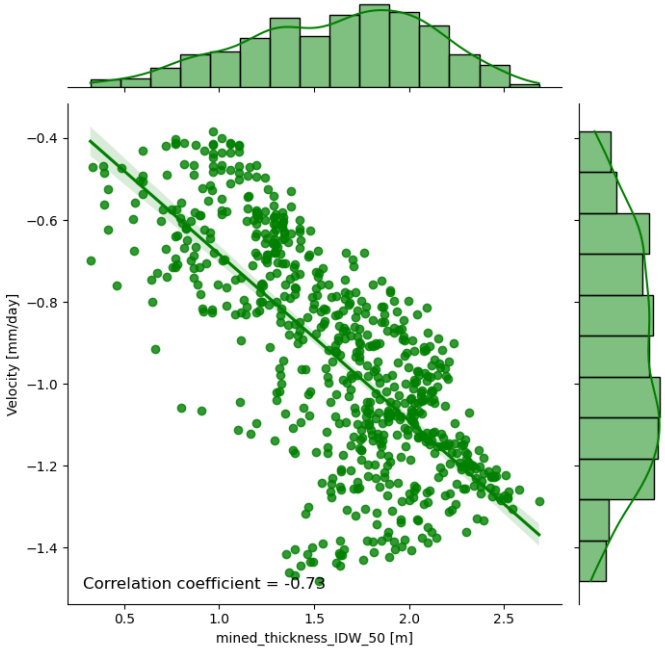


Figure 21. The relationship of the highest subsidence velocities (y-axis) to the spatially averaged (IDW 50 points) thickness of the excavation (x-axis) after elimination of measurement points for which mining took place before the collection of the first InSAR data (end of 2014) and points from the south. Correlation coefficient = -0.73; it is statistically significant—p-value = 8.2×10^{-113}.

After eliminating the southern points adjacent to the locations in which mining operations were active before the first InSAR data acquisition, the correlation coefficient of the mined thickness and the highest subsidence rates reaches -0.73 and is statistically significant. This fact means that the greater the thickness of the excavations, the higher the

rates of subsidence observed above them.

This relationship was identified using the elimination method, but it was a manual and time-consuming process. The high significance of this parameter for the machine model and its SHAP value means that the model was able to automatically find this relationship in combination with the time remaining to excavation closure and/or other parameters and assign high significance to it. The proposed approach to identifying variables that significantly influence mining-induced ground deformations can, under certain conditions, complement numerical methods.

5. Discussion

This study presents a new methodology for analyzing the relevance of geologic-mining parameters affecting ground surface movements. The proposed approach is based on large SAR datasets covering several years of data acquisition with high temporal frequency. The SAR time series alongside the geological-mining data form the core of the machine learning model. Significance analyses were performed using the SHAP algorithm. We find that this approach to mining deformation is relatively new, and the number of publications on such an issue is negligible. The few papers using the SHAP algorithm and/or SAR data from the broader geohazards area do not strictly deal with surface deformation caused by underground mining activities.

The SHAP method was chosen to provide information about the relevance of each parameter. Unlike other methods, such as the local interpretable model-agnostic explanations (Lime) or "Explain Like I'm 5" (ELI5), it takes into account global relevance in combination with the interaction of a parameter with the others. Lime [60] only provides information regarding local relevance (i.e., that which is relevant to only one instance of the input data). In contrast, ELI5 [61] does not take into account the interaction between parameters based on game theory, as in SHAP. There are other tools like Yellowbrick [62], but in this case it is only useful for data visualization and does not provide any information about the relevance of parameters (neither local nor global). For data visualization, in addition to SHAP, we used Python libraries: Matplotlib [63], seaborn [64], and Pandas [65]. According to the authors, SHAP is currently the optimal tool for testing the global significance of parameters, as it considers interactions with other parameters. The possibility of global parameter testing, as in our case, has been used in earthquake detection and analysis studies [66,67].

The analyses showed that the thickness_layer_PZ3 layer, which is located about 200 m above the roof of the mined seam, mined_thickness_IDW_50, and the time of mining have the most significant impact on the observed surface subsidence velocities. In addition, two groups of points were identified for which additional analyses were performed. A number of points were found to have very low subsidence velocities regardless of the thickness of the seam directly below them. In contrast, points were identified that show a high correlation of subsidence velocity with the thickness of the excavation. We believe that what is new is to propose a new approach to analyze the significance of geological-mining parameters and to select those that have the most significant impact on the magnitude and spatial extent of ground surface subsidence.

With the help of SHAP values, it was shown that mining parameters, such as the spatially averaged thickness of the deposit (mined_thickness_IDW_50), the time since the liquidation of the deposit at a given measurement point (t0) as well as the spatially averaged one (t0_IDW_50), and the thickness of the PZ3 geological layer have the most influence on ground subsidence over mine excavations.

The correlation coefficient for deposit thickness was not one of the strongest due to the fact that some of the excavations were completed before the first InSAR data were acquired (2014). Only after deeper analysis was it possible to show a correlation between subsidence velocity and this parameter.

In addition, we find that the proposed model was able to detect the nonlinear dependence of the thickness of the excavation on the objective function or that it is not significant for the point in time where the highest subsidence velocities occurred. The observed obser-

vation is subject to further analysis covering not one but several different mining areas.

We believe it is also important to clearly articulate the limitations of using SAR data and ML algorithms in the analysis of subsidence in mining areas. The approach we presented included, as variables, data on geological structure and local tectonic conditions. In terms of mining, the spatial extent of mining, generalized information on the period of parcel mining was taken into account. The mining system used was also taken into account. On the other hand, the proposed approach does not take into account such parameters as the time factor, which refers to the period in which deformations resulting directly from mining will disappear. In addition, the analyzed area is characterized by high activity of induced seismic events, which were also not taken into account in the analyses. In this particular case, mining shocks are related to the geological structure of the region. It is assumed that copper ores in the LGCB area are formed in three types of rocks: Rotliegend and Grauliegend sandstones, Zechstein copper shales, and carbonate rocks. Rocks of the last type, typically found in the roofs of excavations, exhibit high strength and the ability to accumulate elastic energy. Therefore, they facilitate the occurrence of mining tremors.

The authors ultimately plan to modify the ML model, which will also take into account the above-mentioned parameters.

6. Conclusions

Each mining activity causes unfavorable changes in the environment. The form in which mining activities impact the environment depends mainly on the mining method. Forecasting deformations caused by underground mining is an issue related to public safety. This article identifies the variables that have a decisive impact on the extent and range of mining-induced ground surface deformations. The input data consisted of long-term subsidence calculated using the SBAS method and SAR data from the Sentinel 1 mission. The geological variables were identified with the use of machine learning algorithms. The analyses were performed using the SHAP method and the traditional correlation method. The results allow for the following final conclusions:

- The most significant influence on ground subsidence over mine excavations are mining parameters such as the spatially averaged thickness of the deposit and the time since liquidation of the deposit;
- From the group of geological variables, the thickness of the PZ3 layer had the most significant impact on the velocity of the ground subsidence;
- Subsidence rate calculated from SAR data can be used as a target function for machine models;
- SHAP value analyses obtained from machine learning models can help to quickly identify mining and geological parameters that have the greatest impact on subsidence rates in mining areas, and additionally to identify nonlinear relationships;
- The proposed methodology can be employed in planning both mining operations and mine closure in such a manner that the environmental impact is minimized (in accordance with the environmental, social, and governance framework).

The combination of SAR data, machine learning, and the SHAP method proposed in this article is a completely new approach to the monitoring of the impact of mining activity on ground surface. The method for quickly determining which of the geological and mining parameters has a decisive impact on ground surface deformations also has an equally important application potential. The possibility to examine the relationships between various parameters, including nonlinear relationships, opens new directions of research in this area.

Author Contributions: Conceptualization, K.C., W.M., E.W., P.K. and R.R.; Formal analysis, K.C. and W.M.; Investigation, K.C., W.M., E.W., P.K. and R.R.; Methodology, K.C. and W.M.; Project administration, K.C. and W.M.; Resources, K.C. and W.M.; Validation, P.K.; Visualization, K.C. and W.M.; Writing—original draft, K.C. and W.M.; Writing—review and editing, K.C. and W.M. All authors have read and agreed to the published version of the manuscript.

Funding: Calculations have been carried out using resources provided by Wroclaw Centre for Networking and Supercomputing (https://wcss.pl), grant No. 345 and servers from trainAI sp z o.o., accessed from 2 November to 20 December 2023.

Data Availability Statement: The raw data supporting the conclusions of this article will be made available by the authors on request.

Conflicts of Interest: Author Konrad Cieślik was employed by the company trainAI. Authors Ewa Warchala, Paweł Kosydor and Robert Rożek were employed by the company KGHM. The remaining authors declare that the research was conducted in the absence of any commercial or financial relationships that could be construed as a potential conflict of interest.

References

1. Grygierek, M.; Kalisz, P. Influence of mining operations on road pavement and sewer system—Selected case studies. *J. Sustain. Min.* **2018**, *17*, 56–67. [CrossRef]
2. Diao, X.; Wu, K.; Chen, R.; Yang, J. Identifying the Cause of Abnormal Building Damage in Mining Subsidence Areas Using InSAR Technology. *IEEE Access* **2019**, *7*, 172296–172304. [CrossRef]
3. Blachowski, J.; Milczarek, W.; Cacoń, S. Project of a rock mass surface deformation monitoring system in the Walbrzych Coal Basin. *Acta Geodyn. Geomater.* **2010**, *7*, 349–354.
4. Samsonov, S.; Smets, B.; D'Oreye, N.; Smets, B. Ground deformation associated with post-mining activity at the French—German border revealed by novel InSAR time series method. *Int. J. Appl. Earth Obs. Geoinf.* **2013**, *23*, 142–154. [CrossRef]
5. Brown, N.; Kaloustian, S.; Roeckle, M. Monitoring of Open Pit Mines Using Combined GNSS Satellite Receivers and Robotic Total Stations. In Proceedings of the 2007 International Symposium on Rock Slope Stability in Open Pit Mining and Civil Engineering, Australian Centre for Geomechanics, Slope 2007, Perth, SCT, Australia, 12–14 September 2007. [CrossRef]
6. Jing-xiang, G.; Hong, H. Advanced GNSS technology of mining deformation monitoring. *Procedia Earth Planet. Sci.* **2009**, *1*, 1081–1088. [CrossRef]
7. Bo, H.; Li, Y.; Tan, X.; Dong, Z.; Zheng, G.; Wang, Q.; Yu, K. Estimation of Ground Subsidence Deformation Induced by Underground Coal Mining with GNSS-IR. *Remote Sens.* **2022**, *15*, 96. [CrossRef]
8. Ren, H.; Zhao, Y.; Xiao, W.; Hu, Z. A review of UAV monitoring in mining areas: Current status and future perspectives. *Int. J. Coal Sci. Technol.* **2019**, *6*, 320–333. [CrossRef]
9. Ćwiąkała, P.; Gruszczyński, W.; Stoch, T.; Puniach, E.; Mrocheń, D.; Matwij, W.; Matwij, K.; Nędzka, M.; Sopata, P.; Wójcik, A. UAV Applications for Determination of Land Deformations Caused by Underground Mining. *Remote Sens.* **2020**, *12*, 1733. [CrossRef]
10. Puniach, E.; Gruszczyński, W.; Ćwiąkała, P.; Matwij, W. Application of UAV-based orthomosaics for determination of horizontal displacement caused by underground mining. *ISPRS J. Photogramm. Remote Sens.* **2021**, *174*, 282–303. [CrossRef]
11. Chen, B.; Deng, K.; Fan, H.; Hao, M. Large-scale deformation monitoring in mining area by D-InSAR and 3D laser scanning technology integration. *Int. J. Min. Sci. Technol.* **2013**, *23*, 555–561. [CrossRef]
12. Maciaszek, J.; Madusiok, D.; Matwij, W. The comparison of the results of laser scanning and classical surveying methods of measuring the area and volume in the chapel of St. Kinga in the salt mine of Bochnia. *Geol. Geophys. Environ.* **2013**, *39*, 211. [CrossRef]
13. Zheng, J.; Yao, W.; Lin, X.; Ma, B.; Bai, L. An Accurate Digital Subsidence Model for Deformation Detection of Coal Mining Areas Using a UAV-Based LiDAR. *Remote Sens.* **2022**, *14*, 421. [CrossRef]
14. Dong, Y.; Wang, D.; Liu, F.; Wang, J. A New Data Processing Method for High-Precision Mining Subsidence Measurement Using Airborne LiDAR. *Front. Earth Sci.* **2022**, *10*, 858050. [CrossRef]
15. Kim, J.s.; Kim, D.J.; Kim, S.W.; Won, J.S.; Moon, W.M. Monitoring of urban land surface subsidence using PSInSAR. *Geosci. J.* **2007**, *11*, 59–73. [CrossRef]
16. Blachowski, J. Application of satellite radar interferometry (PSINSAR) in analysis of secondary surface deformations in mining areas case studies from Czech Republic and Poland. *Acta Geodyn. Geomater.* **2018**, *15*, 173–185. [CrossRef]
17. Zhou, C.; Lan, H.; Gong, H.; Zhang, Y.; Warner, T.A.; Clague, J.J.; Wu, Y. Reduced rate of land subsidence since 2016 in Beijing, China: Evidence from Tomo-PSInSAR using RadarSAT-2 and Sentinel-1 datasets. *Int. J. Remote Sens.* **2019**, *41*, 1259–1285. [CrossRef]
18. Anil, J.; Kumar, K.; Ram, S.; Chatterjee, S.; Gorai, A.K. Monitoring of Subsidence Over a Continuous Miner-Based Coal Mine Caving Panels Using PS-InSAR Technique. *Mining, Metall. Explor.* **2023**, *40*, 719–736. [CrossRef]
19. Kopec, A. Long-term monitoring of the impact of the impact of mining operations on the ground surface at the regional scale based on the InSAR-SBAS technique, the Upper Silesian Coal Basin (Poland). Case study. *Acta Geodyn. Geomater.* **2021**, *19*, 93–110. [CrossRef]
20. Milczarek, W. Application of a Small Baseline Subset Time Series Method with Atmospheric Correction in Monitoring Results of Mining Activity on Ground Surface and in Detecting Induced Seismic Events. *Remote Sens.* **2019**, *11*, 1008. [CrossRef]
21. Wang, L.; Deng, K.; Zheng, M. Research on ground deformation monitoring method in mining areas using the probability integral model fusion D-InSAR, sub-band InSAR and offset-tracking. *Int. J. Appl. Earth Obs. Geoinf.* **2020**, *85*, 101981. [CrossRef]

22. Chen, Y.; Tong, Y.; Tan, K. Coal Mining Deformation Monitoring Using SBAS-InSAR and Offset Tracking: A Case Study of Yu County, China. *IEEE J. Sel. Top. Appl. Earth Obs. Remote Sens.* **2020**, *13*, 6077–6087. [CrossRef]
23. Carlà, T.; Farina, P.; Intrieri, E.; Ketizmen, H.; Casagli, N. Integration of ground-based radar and satellite InSAR data for the analysis of an unexpected slope failure in an open-pit mine. *Eng. Geol.* **2018**, *235*, 39–52. [CrossRef]
24. Heddallikar, A.; Pinto, R.; Kothari, H.; James, J.; Rao, Y.; Sajjad, T. Initial Results of Ground based SAR Experiment in an Opencast Coal Mine for Slope Stability Monitoring. In Proceedings of the 2022 IEEE Microwaves, Antennas, and Propagation Conference (MAPCON), Bangalore, India, 12–16 December 2022. [CrossRef]
25. Anantrasirichai, N.; Biggs, J.; Albino, F.; Bull, D. A deep learning approach to detecting volcano deformation from satellite imagery using synthetic datasets. *Remote Sens. Environ.* **2019**, *230*, 111179. [CrossRef]
26. Hill, P.; Biggs, J.; Ponce-López, V.; Bull, D. Time-Series Prediction Approaches to Forecasting Deformation in Sentinel-1 InSAR Data. *J. Geophys. Res. Solid Earth* **2021**, *126*, e2020JB020176. [CrossRef]
27. Rouet-Leduc, B.; Jolivet, R.; Dalaison, M.; Johnson, P.A.; Hulbert, C. Autonomous extraction of millimeter-scale deformation in InSAR time series using deep learning. *Nat. Commun.* **2021**, *12*, 6480. [CrossRef] [PubMed]
28. Cieślik, K.; Milczarek, W. Application of Machine Learning in Forecasting the Impact of Mining Deformation: A Case Study of Underground Copper Mines in Poland. *Remote Sens.* **2022**, *14*, 4755. [CrossRef]
29. Ma, F.; Sui, L.; Lian, W. Prediction of Mine Subsidence Based on InSAR Technology and the LSTM Algorithm: A Case Study of the Shigouyi Coalfield, Ningxia (China). *Remote Sens.* **2023**, *15*, 2755. [CrossRef]
30. Mirmazloumi, S.M.; Wassie, Y.; Nava, L.; Cuevas-González, M.; Crosetto, M.; Monserrat, O. InSAR time series and LSTM model to support early warning detection tools of ground instabilities: Mining site case studies. *Bull. Eng. Geol. Environ.* **2023**, *82*, 374. [CrossRef]
31. Long, S.; Liu, M.; Xiong, C.; Li, T.; Wu, W.; Ding, H.; Zhang, L.; Zhu, C.; Lu, S. Research on Prediction of Surface Deformation in Mining Areas Based on TPE-Optimized Integrated Models and Multi-Temporal InSAR. *Remote Sens.* **2023**, *15*, 5546. [CrossRef]
32. Vyazmensky, A.; Stead, D.; Elmo, D.; Moss, A. Numerical Analysis of Block Caving-Induced Instability in Large Open Pit Slopes: A Finite Element/Discrete Element Approach. *Rock Mech. Rock Eng.* **2009**, *43*, 21–39. [CrossRef]
33. Sikora, P.; Wesołowski, M. Numerical assessment of the influence of former mining activities and plasticity of rock mass on deformations of terrain surface. *Int. J. Min. Sci. Technol.* **2021**, *31*, 209–214. [CrossRef]
34. Blachowski, J.; Cacoń, S.; Milczarek, W. Analysis of post-mining ground deformations caused by underground Coal extraction in complicated geological conditions. *Acta Geodyn. Geomater.* **2009**, *6*, 351–357.
35. Dudek, M.; Tajduś, K. FEM for prediction of surface deformations induced by flooding of steeply inclined mining seams. *Geomech. Energy Environ.* **2021**, *28*, 100254. [CrossRef]
36. Ju, Y.; Wang, Y.; Su, C.; Zhang, D.; Ren, Z. Numerical analysis of the dynamic evolution of mining-induced stresses and fractures in multilayered rock strata using continuum-based discrete element methods. *Int. J. Rock Mech. Min. Sci.* **2019**, *113*, 191–210. [CrossRef]
37. Zhang, Z.; Mei, G.; Xu, N. A geometrically and locally adaptive remeshing method for finite difference modeling of mining-induced surface subsidence. *J. Rock Mech. Geotech. Eng.* **2022**, *14*, 219–231. [CrossRef]
38. Chen, R.; Zhang, P.; Wu, H.; Wang, Z.; Zhong, Z. Prediction of shield tunneling-induced ground settlement using machine learning techniques. *Front. Struct. Civ. Eng.* **2019**, *13*, 1363–1378. [CrossRef]
39. Sheil, B.B.; Suryasentana, S.K.; Mooney, M.A.; Zhu, H. Machine learning to inform tunnelling operations: Recent advances and future trends. *Proc. Inst. Civ. Eng.-Smart Infrastruct. Constr.* **2020**, *173*, 74–95. [CrossRef]
40. Tang, L.; Na, S. Comparison of machine learning methods for ground settlement prediction with different tunneling datasets. *J. Rock Mech. Geotech. Eng.* **2021**, *13*, 1274–1289. [CrossRef]
41. Cho, E.; Jacobs, J.M.; Jia, X.; Kraatz, S. Identifying Subsurface Drainage using Satellite Big Data and Machine Learning via Google Earth Engine. *Water Resour. Res.* **2019**, *55*, 8028–8045. [CrossRef]
42. Vu, V.T.; Nguyen, H.D.; Vu, P.L.; Ha, M.C.; Bui, V.D.; Nguyen, T.O.; Hoang, V.H.; Nguyen, T.K.H. Predicting land use effects on flood susceptibility using machine learning and remote sensing in coastal Vietnam. *Water Pract. Technol.* **2023**, *18*, 1543–1555. [CrossRef]
43. Hussaine, S.M.; Mu, L. Intelligent Prediction of Maximum Ground Settlement Induced by EPB Shield Tunneling Using Automated Machine Learning Techniques. *Mathematics* **2022**, *10*, 4637. [CrossRef]
44. Kannangara, K.P.M.; Zhou, W.; Ding, Z.; Hong, Z. Investigation of feature contribution to shield tunneling-induced settlement using Shapley additive explanations method. *J. Rock Mech. Geotech. Eng.* **2022**, *14*, 1052–1063. [CrossRef]
45. Ali, N.; Chen, J.; Fu, X.; Ali, R.; Hussain, M.A.; Daud, H.; Hussain, J.; Altalbe, A. Integrating Machine Learning Ensembles for Landslide Susceptibility Mapping in Northern Pakistan. *Remote Sens.* **2024**, *16*, 988. [CrossRef]
46. Naghibi, S.A.; Khodaei, B.; Hashemi, H. An integrated InSAR-machine learning approach for ground deformation rate modeling in arid areas. *J. Hydrol.* **2022**, *608*, 127627. [CrossRef]
47. Berardino, P.; Fornaro, G.; Lanari, R.; Sansosti, E. A new algorithm for surface deformation monitoring based on small baseline differential {SAR} interferograms. *IEEE Trans. Geosci. Remote Sens.* **2002**, *40*, 2375–2383. [CrossRef]
48. Saarela, M.; Jauhiainen, S. Comparison of feature importance measures as explanations for classification models. *SN Appl. Sci.* **2021**, *3*, 272. [CrossRef]

49. Sandwell, D.; Mellors, R.; Tong, X.; Wei, M.; Wessel, P. Open radar interferometry software for mapping surface Deformation. *Eos. Trans. Am. Geophys. Union* **2011**, *92*, 234–234. [CrossRef]
50. Chen, C.W.; Zebker, H.A. Phase unwrapping for large SAR interferograms: Statistical segmentation and generalized network models. *IEEE Trans. Geosci. Remote Sens.* **2002**, *40*, 1709–1719. [CrossRef]
51. Farr, T.; Rosen, P.A.; Caro, E.; Crippen, R.; Duren, R.; Hensley, S.; Kobrick, M.; Paller, M.; Rodriguez, E.; Roth, L.; et al. The shuttle radar topography mission. *Rev. Geophys.* **2007**, *45*, 1–33. [CrossRef]
52. Yu, C.; Li, Z.; Penna, N.T.; Crippa, P. Generic Atmospheric Correction Model for Interferometric Synthetic Aperture Radar Observations. *J. Geophys. Res. Solid Earth* **2018**, *123*, 9202–9222. [CrossRef]
53. Milczarek, W.; Kopeć, A.; Głąbicki, D. Estimation of Tropospheric and Ionospheric Delay in DInSAR Calculations: Case Study of Areas Showing (Natural and Induced) Seismic Activity. *Remote Sens.* **2019**, *11*, 621. [CrossRef]
54. Milczarek, W.; Kopeć, A.; Głąbicki, D.; Bugajska, N. Induced Seismic Events—Distribution of Ground Surface Displacements Based on InSAR Methods and Mogi and Yang Models. *Remote Sens.* **2021**, *13*, 1451. [CrossRef]
55. Piestrzyński, A. (Ed.) *Monografia KGHM Polska Miedź S.A.*, 2nd ed.; KGHM Cuprum: Wrocław, Poland, 2007.
56. Chen, T.; Guestrin, C. XGBoost: A Scalable Tree Boosting System. In Proceedings of the 22nd acm sigkdd International Conference on Knowledge Discovery and Data Mining, KDD '16, New York, NY, USA, 13–17 August 2016; pp. 785–794. [CrossRef]
57. Lundberg, S.M.; Lee, S.I. A Unified Approach to Interpreting Model Predictions. In Proceedings of the 31st International Conference on Neural Information Processing Systems, NIPS'17, Red Hook, NY, USA, 4–9 December 2017; pp. 4768–4777.
58. Lundberg, S.M.; Erion, G.; Chen, H.; DeGrave, A.; Prutkin, J.M.; Nair, B.; Katz, R.; Himmelfarb, J.; Bansal, N.; Lee, S.I. From local explanations to global understanding with explainable AI for trees. *Nat. Mach. Intell.* **2020**, *2*, 56–67. [CrossRef] [PubMed]
59. Lundberg, S.M.; Erion, G.G.; Lee, S.I. Consistent Individualized Feature Attribution for Tree Ensembles. *arXiv* **2019**, arXiv:1802.03888. [CrossRef]
60. Ribeiro, M.T.; Singh, S.; Guestrin, C. "Why Should I Trust You?": Explaining the Predictions of Any Classifier. In Proceedings of the KDD '16: Proceedings of the 22nd ACM SIGKDD International Conference on Knowledge Discovery and Data Mining, San Francisco, CA, USA, 13–16 August 2016. [CrossRef]
61. ELI5 Contributors. ELI5: A Python Library for Debugging/Inspecting Machine Learning Classifiers and Explaining Their Predictions. Available online: https://eli5.readthedocs.io/en/latest/index.html (accessed on 14 December 2023).
62. Bengfort, B.; Danielsen, N.; Bilbro, R.; Gray, L.; McIntyre, K.; Richardson, G.; Miller, T.; Mayfield, G.; Schafer, P.; Keung, J. *Yellowbrick*, v0.6; ZENODO: Geneve, Switzerland, 2018. [CrossRef]
63. Hunter, J.D. Matplotlib: A 2D Graphics Environment. *Comput. Sci. Eng.* **2007**, *9*, 90–95. [CrossRef]
64. Waskom, M. seaborn: Statistical data visualization. *J. Open Source Softw.* **2021**, *6*, 3021. [CrossRef]
65. McKinney, W. Data Structures for Statistical Computing in Python. In Proceedings of the 9th Python in Science Conference, SciPy, Austin, TX, USA, 28–30 June 2010. [CrossRef]
66. Jena, R.; Pradhan, B.; Gite, S.; Alamri, A.; Park, H.J. A new method to promptly evaluate spatial earthquake probability mapping using an explainable artificial intelligence (XAI) model. *Gondwana Res.* **2023**, *123*, 54–67. [CrossRef]
67. Dang, H.; Wang, Z.; Zhao, D.; Wang, X.; Li, Z.; Wei, D.; Wang, J. Ground motion prediction model for shallow crustal earthquakes in Japan based on XGBoost with Bayesian optimization. *Soil Dyn. Earthq. Eng.* **2024**, *177*, 108391. [CrossRef]

Disclaimer/Publisher's Note: The statements, opinions and data contained in all publications are solely those of the individual author(s) and contributor(s) and not of MDPI and/or the editor(s). MDPI and/or the editor(s) disclaim responsibility for any injury to people or property resulting from any ideas, methods, instructions or products referred to in the content.